Interfacial Engineering of Smart Polymer Self-Assembly Using Doped-Nanostructures for Constructing Stable Nano-Carriers

Arash Arabmarkadeh
Tarbiat Modares University
Nasser Mortezaei
Sharif University of Technology
Mojtaba Mirzaasadi
Islamic Azad University
Amin Hejazi (aminhejazi@abrii.ac.ir)
Agricultural Biotechnology Research Institute of Iran
Amir Sepehri
Islamic Azad University

Research Article

Keywords: PLGA-PEG-Riboflavin, Cancer treatment, Nano materials, Nano-carrier, MD Simulation

Posted Date: April 7th, 2021

DOI: https://doi.org/10.21203/rs.3.rs-387614/v1

Abstract

Nowadays, nanotechnology has been developed in various fields of treatment, including cancer treatment. Since the prevalence of different types of cancer has risen, and currently available cancer treatments such as chemotherapy and radiotherapy may cause serious side effects. In this regard, researchers have made considerable efforts to encourage the creation and make strides in treating this deadly disease. Meanwhile, nanotechnology has become widespread, and various nanomaterials, including nanoparticles, have been extensively used to transfer the drug to the targeted sites. Recently, many drug delivery systems have been developed based on nanoparticles, and various substances have been employed as drug stimulants or enhancers to improve the treatment effectiveness, stability, and safety of anticancer drugs. In this paper, the drug delivery capability of three new categories of carbon nanoparticles (i.e., Fullerenes, nanosheets, and Carbon Nano Tubes (CNTs)) was investigated by Molecular Dynamics (MD) simulation. Energy, Gyration Radius (Rg), Hydrogen bond (H-Bond), Radial Distribution Function (RDF), and Solvent Accessible Surface Area (SASA) analyses have been used to compare the studied nanoparticles. The Boron Carbon Nitride (BCN) nanosheet simulation exhibited the lowest drug particle Contact Area, the highest RDF, the most inferior reduction in the Rg, the highest number of H-Bonds, and the highest drug adsorption energy. Thus, BCN nanosheet was introduced as the best nanoparticle for drug delivery purposes.

Introduction

Nowadays, cancer has become one of the most common diseases worldwide[1]. Cancer is a consequence of the mutation in the cells. As mutated cells multiply more rapidly than normal ones, they can allocate more nutrients and oxygen, thus making supplements scares for the normal cells[2,3]. Moreover, transferring the drug to the cancer cell sites is a significant challenge in cancer treatment. Due to the fact that transferring anticancer drugs to the entire body may cause many complications; in addition, some cancer cells may develop resistance against anticancer drugs during chemotherapy. Elevation of the drug dose and co-administration of several drugs have been employed to resolve this problem; both these solutions, however, can increase the drug toxicity. Although anticancer drugs can kill cancer cells, they can also interfere with the growth and division of healthy cells. Impaired development of healthy cells may result in severe complications. When these drugs affect cancer cells, they temporarily reduce the number of blood cells, increasing the risk of infection and fatigue in the patient which in term give rises to other diseases [4–7].

Drug transmission is a vital part of medicine and treatment. Drug delivery systems (DDS) have been created to make strides in the therapeutic properties and pharmacological of drugs utilized among cancer patients [8]. DDS is capable of releasing a specific amount of drug in a particular site, hence, reducing the side effects while enhancing the drug efficacy. Furthermore, DDS can increase the chance of drug uptake by cancer cells, prevent premature breakdown of the drug in the body, and maintain drug concentration

during treatment by controlling the rate of drug release[9,10]. To prevent side effects, a wide variety of DDS systems have been developed for the drug accumulates in the target site[11].

In recent years, increasing attention has been paid to nanostructured carriers' preparation for drug delivery, as these structures are smaller than the cell and can control and slow down the drug release and protect the drug molecule. The ability of the DDSs to overcome the biological barriers can increase the drug persistence in the bloodstream. In this regard, targeted drug delivery and biocompatibility can be considered the crucial advantages of drug delivery systems[12]. Over the past half-century, advancements in polymer science, chemistry, biology, and mechanical and physical sciences have resulted in the development of various nano-carriers with unique features and versatile performances. In general, pharmaceutical carriers can be classified into two main groups: organic and inorganic carriers.

Various materials such as polymers, metal particles, and lipids have been used to fabricate nano-carriers to transfer drugs. Nano-carrier-based drug delivery systems have now entered the global pharmaceutical market, and their application in drug delivery is increasing day-by-day and nanoparticles have become very popular in various fields of biology and medicine. Since these nanoparticles size are in the range of 100 nm, they can be loaded with a wide range of drugs such as small hydrophobic and hydrophobic drugs, vaccines, and biological molecules [13–16]. Moreover, nanoparticles can likewise improve treatment and diagnosis. In this regard, Carbon Nano Tubes (CNTs) have been utilized as nano-carriers to deliver the drug to the target site[17,18]. Due to the small sizes, these particles can easily pass across the cell membranes and biological barriers. They also possess a high surface area and their surfaces can be modified by various functional groups. This in turn yields to enhance their solubility and biocompatibility, and the conductivity of different materials. These nano-carriers can carry other biological molecules such as proteins, DNA, and pharmaceutical agents loaded on their surface or inside the porous of the structures. Simultaneous targeting and transfer of two or more compounds is another essential feature of these particles [19–21]. The most common nano-carriers are in the form of polymers. For the controlled drug release, these polymers must be biocompatible and non-toxic with no leak or impurity. Physically, they must be well-structured with the desired half-life. Polymers used in the manufacturing of polymer nanoparticles can be synthetic or natural. Polymeric nanoparticles are frequently chosen from biodegradable sorts. The advantage of using polymer nanoparticles lies in their high stability and scalability. The Nano-carriers transfer the required drugs in two ways: 1- Carrying the imprisoned agents (encapsulation) 2- delivering the drugs absorbed on the nanoparticle surface. Polymer nanoparticles are small-sized stable colloidal systems. The drug is either physically distributed in polymer nanoparticles or chemically bonded to its main polymer chain. Increasing the solubility and stability of drugs is one of the advantages of using polymer nanoparticles. Therefore, polymer nanoparticles are among the most widely used drug delivery systems [22–25].

So far, a wide diversity of polymers have been used as polymer nanoparticles. In polymer nanoparticles' synthesis, Poly (lactic-co-glycolic acid) (PLGA) is used. European Medicines Agency (EMA) and the Food and Drug Administration (FDA) approved the biocompatibility and biodegradability of PLGA[26–28]. Poly

(ethylene glycol) (PEG) is a chemical compound made by repeating ethylene glycol units. PEG has found numerous medical industry applications; thanks to its non-toxicity, biocompatibility, and water-solubility, its pharmaceutical and biomedical applications are continuously expanding [29–31].

Riboflavin is one of the vitamin B family, which plays an essential role in several body activities, including cell growth. Riboflavin can naturally be found in milk, meat, eggs, fortified flour nuts, and green vegetables. The cancer cells have exhibited too high riboflavin uptake. Thus, it can significantly contribute to delivering the drug to cancer cells. In this context, scientists combined riboflavin to anticancer drugs and mounted it onto a carrier such as nanoparticles to treat cancer cells. Cancer cell membrane receptors can absorb riboflavin [32–34].

A successful transport of the drug to the cancer cell requires strong adsorption between the drug and the nanoparticle. The use of MD simulation makes it possible to investigate the adsorption capacity of drugs by different nano-carriers. As the experimental evaluation of DDS performance could be complicated, time-consuming, and expensive, and the molecular dynamics (MD) simulation is an excellent tool capable of examining the drug- Nano-carrier interactions under different conditions. In this paper, the transfer of Doxorubicin (DOX) along with riboflavin by carbon nanoparticles and PEG and PLGA polymeric nanoparticles was investigated for the first time. Rezvantalab et al. Reported the best concentrations of PLGA and PEG polymers for drug delivery to the target area at a ratio of 8:2 [35]. In this paper, PLGA and PEG are combined at a ratio of 8:2. Fullerene, nanosheets, CNTs, and their derivatives have also been used as part of the Nano-carrier. The energy, Hydrogen bond (H-bond), Gyration Radius (Rg), Solvent Accessible Surface Area (SASA), and Radial Distribution Function (RDF) analyses were employed to analyze the adsorption power of various simulated Nano-carriers.

Methods

The molecular structure of DOX was obtained from rcsb.org. The initial molecular systems of Fullerene, nanosheet, and CNTs were designed by Nanotube_Modeler_1.7.9 [36,37]. The molecular systems of Boron Carbon Nitride (BCN) nanosheet, BCN nanotube, and BCN Fullerene were developed by Avogadro software by adding N and B atoms molecular structure of the mentioned systems. Replacing 10% of carbon atoms with nitrogen atoms create Nitrogen-doped (N doped) Graphene, N doped nanotube, and N doped Fullerene molecular structures. The Phosphorus doped (P doped) Graphene, P doped nanotube, and P doped Fullerene molecular structures were created by Avogadro software by adding phosphorus atoms to the molecular structure of nanosheets, CNTs, and Fullerene. Then, the molecular structures were optimized with Gaussian 09 [38,39]software. To calculate the charge distribution of atoms, the Density Functional Theory (DFT) method was used through the B3LYP functional and 6-31G basis set.

The topology of these two-dimensional structures was then obtained by applying esp charges calculated from the Gaussian software and by the x2top command for the OPLSAA force field [40,41]. The size of the simulation boxes was set 3 x 3 x 30 nm^3. We then placed the built-in molecular structures in the simulation boxes and add 30600 (SPC / E water model) water molecules to each box.

We performed the simulation in 4 steps. Initially, we did the optimization at 50,000 2-fs steps, followed by the optimization phase's energy level was set at 10kj/mol. Then an NVT simulation was performed for 500 ps to balance the simulation box's temperature at 300 K by the V_rescale algorithm [42–44]. In the NPT stage, the simulation box pressure was balanced at 1 bar by the parrinello_rahman algorithm[45–47]in at 500 ps. In the end, considering the H-bond, cut-off radius of 1.4 nm, the last simulation was performed by the lincs algorithm at 100 ns. Energy, Rg, H-bond, RDF, and SASA analyses were also performed for different simulations.

Results

Investigation of polymer micelle Compactness by using analysis of Rg:

In this paper, the polymer micelles are applied to transmit the drug. The higher the compaction of micelle particles around the drug, the more likely the drug transfer to the target cells. Accumulation of polymer micelles around the drug prevents the drug from release to unwanted regions. Lower final Rg (compared to the initial Rg) indicates better drug surroundings by micelles. Figure 1 shows the accumulation of polymers by a reduction in the Rg after 100 ns. Condensation of the polymer reduced the oscillations of the polymer particles. The compactness of polymer particles also declined the Rg and further stabilized the system. For comparing the simulated systems' stability, the difference between the initial and final Rg was studied. One of the essential analyzes in polymer simulations is the Rg analysis, since Rg analysis indicates the accumulation of polymer particles around its center of gravity at different times. The lower the Rg, the greater the accumulation of particles around the gravity center.[48–52]; reflecting that the drug is surrounded by micelles for transfer to the body. In case the (r_i-r_{cm}) communicates the separate between the particle i and the center of mass of the particle, at that point the Rg from the connection 1 is calculated.

$$Rg = (1/N_i \sum (r_i - r_{cm})^{2)\,½} \qquad (1)$$

Table 1 shows the difference between the initial and final Rg for BCN Fullerene, Fullerene, N doped Fullerene, and P doped Fullerene simulations. Figure 2 indicates the Rg values for the same materials are plotted versus the simulation time. Consequently, Fig. 5 depicts the values of the final Rg, which shows the lowest value in the BCN nanosheet simulation. The lower final Rg in the BCN nanosheet simulation indicates more reduction in the Rg in this system. The Rg diagrams of BCN Fullerene and P doped Fullerene simulations show the variations in their Rg. However, Fullerene exhibits an increasing trend in the Rg. Despite of a decreasing trend in the Rg value of the N doped Fullerene during 5–60 ns interval, a sudden increase in the Rg at 60–80 ns range prevented a significant reduction in the final Rg. The BCN Fullerene shows the highest reduction in the final Rg. Polymers exhibit the highest accumulation in BCN Fullerene simulation with a decrease in the Rg of 1.16263 nm. In BCN Fullerene, the drug was more surrounded by polymer micelles giving rise to higher stability. A 0.9833 nm reduction was detected in the Rg of the P doped Fullerene. After the BCN Fullerene simulation, the highest accumulation of polymer

particles occurred in the P doped Fullerene simulation. Among Fullerene systems, BCN Fullerene polymeric micelle exhibits the most increasing stability for drug delivery.

Table 2 shows the difference between the initial and final Rg for BCN nanosheet, Graphene, N doped Graphene, and P doped Graphene systems. Figure 4 also presents the graph of the Rg vs. the simulation time, while Fig. 5 shows the values of the final Rg. The final Rg has the lowest value in the BCN nanosheet simulation, reflecting a higher Rg reduction. A sudden increase in the Rg occurring in 90–95 ns for the BCN nanosheet and P doped Graphene systems failed to prevent a reduction in the final Rg in these simulations. Although the Rg was increasing through th simulation, a sudden decrease in the Rg at the interval of 95–100 ns affected the final Rg compared to its initial value. BCN nanosheet simulation offered the most considerable reduction in the final Rg. Polymers showed the highest accumulation in BCN nanosheet simulation, with Rg reduction of 1.40905 nm. The proliferation of polymer particles in the BCN nanosheet system reduced the polymer particles' oscillations and increased the simulated system's stability. In BCN nanosheet, the drug was more surrounded by polymer micelles and hence reach more stability. The reduction in the Rg of the P doped Graphene simulation was 1.27934 nm. After the BCN nanosheet, the highest accumulation of polymer particles occurred in the P doped Graphene system. Thus, among nanosheets, BCN nanosheet drug delivery is most stable.

Table 3 shows the difference between the initial and final Rg of BCN nanotube, CNT, N doped nanotube, and P doped nanotube simulations. Figure 6 also demonstrates the Rg values vs. the simulation time, while Fig. 7 shows the final Rg values. The lowest final Rg was obtained in BCN nanotube, indicating a higher reduction of Rg in this system. The Rg value for N doped nanotube and P doped nanotube systems increase over the simulation time. A significant enhancement was observed in the Rg of N doped nanotube in the 35–60 ns interval. In N doped nanotube and P doped nanotube simulations, the final Rg value increased compared to their initial values. However, the Rg diagram in CNT systems shows a decreasing trend most of the time. The Rg dramatically increased in the BCN nanotube in 30–55 ns interval, but a sudden decrease in the Rg in 85–100 ns affected the final Rg compared to its initial value. BCN nanotube exhibited the most considerable reduction in the final Rg. Polymers have the highest accumulation in BCN nanotube simulation with a 1.17895-nm reduction in the Rg. The accumulation of polymer particles in the BCN nanotube reduces the polymer particles' oscillations and increases the stability of the system. As a result, polymer micelles more surrounded the drug; thus it is more stable. The reduction in the Rg in the CNT simulation was 0.91054 nm. After the BCN nanotube, the highest accumulation of polymer particles occurred in the CNT simulation. Among the simulated CNTs, drug delivery by polymer micelle in BCN nanotube has the best stability.

The reduction in the Rg of the BCN nanosheet, BCN nanotube, and BCN Fullerene was 1.40905, 1.17895, and 1.16263 nm, respectively. BCN nanosheet exhibited the most massive reduction in the Rg value among all the simulated materials. The most significant decrease in the Rg occurred in BCN nanosheet which lead to the highest accumulation of polymer particles around the polymers' center of gravity. A successful delivery of the drug requires the drug to be surrounded by polymer micelles and the simulated BCN nanosheet, was well covered the drug. Moreover, the higher accumulation of polymer particles in the

BCN nanosheet simulation results in fewer oscillations of the polymer particles and, hence, it increases the simulated system's stability. After BCN nanosheet, the highest accumulation of polymer particles occurred in BCN nanotube and BCN Fullerene simulations, respectively. Based on the Rg analysis, BCN nanosheet, BCN nanotube, and BCN Fullerene are the best nanoparticles for drug delivery purposes.

Investigation of drug-Nano-carrier hydrogen interactions:

Hydrogen bonding is the strongest intermolecular bond. Hydrogen atoms can form H-bonds in small atoms with high electron affinities such as oxygen and nitrogen. The number of H-bonds between the molecules in the simulation is a good indicator of the simulated systems' interactions. The high hydrogen bonding indicates strong intermolecular interactions. A strong drug-carrier interaction can result in proper drug transfer while preventing drug release in unwanted sites. A strong interaction should be formed between the drug and the polymeric nano-carrier to transfer the drug to target cells [53–55]. In this regard, the H-bond analysis can examine the number of H-bonds formed during the simulation time.

Table 4 shows the mean number of H-bonds between drug and polymer micelles during 100 ns of simulation for BCN Fullerene, Fullerene, N doped Fullerene, and P doped Fullerene systems. Over time, more H-bonds formes between drug and micelle in the BCN Fullerene system. Followed by BCN Fullerene, P doped Fullerene, N doped Fullerene, and Fullerene systems in the term of the number of H-bonds. BCN Fullerene provides better hydrogen bonding conditions between the drug and micelle, suggesting stronger micelle-drug, further enhancing the stable drug transfer to the targeted site. Among Fullerenes, BCN Fullerene provides the best conditions for drug delivery.

Table 5 shows the average number of H-bonds formed between drug and polymer micelles over 100 ns of simulations for BCN nanosheet, Graphene, N doped Graphene, and P doped Graphene systems. Over time, more H-bonds formed between the drug and the micelle in the BCN nanosheet system. After this system, P doped Graphene and N doped Graphene showes the highest H-Bonds, respectively. BCN nanosheet offered better conditions for hydrogen bonding between drug and micelle. The greater the number of H-Bonds, the stronger the micelle-drug interactions. Hence, the drug transfer to the target site become more stable. Among the studied nanosheet, BCN nanosheet exhibited the best drug delivery conditions.

Table 6 shows the mean number of H-Bonds between drug and polymer micelles during 100 ns of simulation for BCN nanotube, CNT, N doped nanotube, and P doped nanotube systems. Over time, more H-bonds were formed between drug and micelle in the BCN nanotube system. After that, the highest number of H-bonds were found in the CNT, N doped nanotube, and P doped nanotube, respectively. BCN nanotube provided better conditions for hydrogen bonding, reflecting stronger micelle-drug interactions. Stronger micelle-drug interaction can further enhance the stable drug transfer to the target site. Among CNTs, BCN Nanotube offered the best drug delivery conditions.

The average number of H-Bonds in BCN nanosheet, BCN nanotube, and BCN Fullerene simulations were 3.972, 2.63, and 2.207, respectively. More H-bonds were formed in the BCN nanosheet system; thus, this system can offer the best hydrogen bonding conditions between micelles and drugs. The improved

conditions for hydrogen bonding in the BCN nanosheet simulation can strengthen micelle-drug interactions. Based on the H-bond analysis, BCN nanosheet is the best carbon-based system for targeted drug delivery.

Investigation of the ability to absorb drug by nano-carriers:

The nano-carrier's job is to deliver the drug to the targeted area and prevent it from being released in other parts of the body. The stronger the drug and the nano-carrier's attraction, the more the drug is absorbed by the nano-carrier and causes less release in unwanted parts of the body. Better drug adsorption indicates better drug delivery conditions as it reflects stronger interactions between the drug and the nano-carrier. Through RDF analysis, it is possible to study the distribution of molecules relative to a reference. RDF analysis shows the Nano-carriers' ability to absorb the drug. Polymeric micelles and carbon nanoparticles were considered as Nano-carrier in this paper [56–62].

Table 7 shows the maximum RDF values for BCN Fullerene, Fullerene, N doped Fullerene, and P doped Fullerene systems. The BCN Fullerene system exhibites the highest drug uptake with a maximum RDF value of 3.701. After BCN Fullerene, P doped Fullerene, Fullerene, and N doped Fullerene offeres the second, third, and fourth highest drug uptake. The higher drug adsorption by BCN Fullerene shows stronger nano-carrier-drug interactions. The BCN Fullerene system provided better drug-nano-carrier interaction and hence improved the targeted drug delivery.

Table 8 shows the maximum RDF values for BCN nanosheet, N doped Graphene, and P doped Graphene systems. BCN nanosheet system showed the highest drug uptake, with a maximum RDF value of 3.876. After BCN nanosheet, P doped Graphene, Graphene, and N doped Graphene possessed the highest drug uptake, respectively. The BCN nanosheets enhanced drug adsorption, indicates the stronger interactions between the nano-carrier and the drug. Thus, this system can provide stronger for drug- carrier interaction and hence improved targeted drug delivery.

Table 9 shows the maximum RDF values for BCN nanotube, N doped nanotube, and P doped nanotube systems. BCN nanotube offered the highest drug uptake, with a maximum RDF of 3.781. After that, N doped nanotube, and P doped nanotube had the highest drug uptake, respectively. The BCN Nanotube's enhanced drug adsorption indicates the stronger interactions between the nano-carrier and the drug. Thus, this system can provide stronger for drug- carrier interaction and hence improved targeted drug delivery.

The maximum RDF values of BCN nanosheet, BCN nanotube, and BCN Fullerene were 3.876, 3.781, and 3.701, respectively. The BCN nanosheet presented the highest maximum RDF value, suggesting greater drug accumulation around the nano-carrier. After BCN nanosheet, drug aggregation around nano-carriers was highest in BCN nanotube and BCN Fullerene systems, respectively. BCN nanosheet managed to provide better conditions for stronger carrier-drug interaction. According to RDF analysis, BCN nanosheet is the best system for targeted drug delivery.

Contact area of drug particles in the presence of nano-carriers:

Interactions between Nano-carriers and drugs cause Nano-carriers to absorb the drug and reduce the drug particles' contact surface. Further adsorption of the drug by the polymer nanoparticles reduces the drug contact with particles. Lower the average contact area of the drug particles result in better drug accumulation inside the nano-carrier. This in turn yields to better-targeted drug delivery conditions.

By the mean of SASA analysis, it is possible to check the contact area of different material particles. In this paper, we performed SASA analysis to investigate the area of contact between drug particles. Eq. (2) was used to calculate the contact area of drug particles.

$$\text{Contact Area}(t) = \tfrac{1}{2}\ (S(0) - S(t)) \qquad (2)$$

Where, S (0) shows the amount of SASA analysis at the beginning of the simulation while S (t) indicates the amount of SASA analysis at different simulation times. In order to compare the contact area of drug particles for different systems, the mean values obtained from Eq. (2) are used.

Table 8 shows the mean contact area of drug particles over time in BCN Fullerene, N doped Fullerene, and P doped Fullerene systems. The BCN Fullerene system showed the lowest contact area (217,739). P doped Fullerene, N doped Fullerene, and Fullerene systems showed the least contact area, respectively. The lower contact area between drug particles in the BCN Fullerene system suggests a higher drug accumulation in the nano-carrier, leading to better-targeted drug delivery. The BCN Fullerene provided better conditions for the transfer of the drug to the target region.

Table 9 presents the mean contact area of drug particles over time for BCN nanosheet, Graphene, N doped Graphene, and P doped Graphene. The BCN nanosheet exhibits the lowest contact area (214,642), followed by P doped Graphene, Graphene, and N doped Graphene, respectively. The lower contact area between drug particles in the BCN nanosheet system implies a higher drug accumulation in the nano-carrier, leading to improved targeted drug delivery. Among the simulated nanosheet, the BCN nanosheet provided better conditions for drug delivery.

Table 10 shows the mean contact area of drug particles over time for BCN nanotube, CNT, N doped nanotube, and P doped nanotube. The BCN nanotube offered the lowest contact area (216,716), followed by CNT, N doped nanotube, and P doped nanotube, respectively. The lower drug contact area in the BCN nanotube system shows a higher drug accumulation in the nano-carrier, leading to better-targeted drug delivery. Among the simulated CNTs, the BCN nanotube provided excellent conditions for drug transport to the target site.

The mean drug contact area was 214.642, 216.716, and 217.739 for the BCN nanosheet, BCN nanotube, and BCN Fullerene systems, respectively. The BCN nanosheet offered less contact area. In the case of the BCN nanosheet system, the lower contact area means the highest drug accumulation in the Nano-carrier,

implying better drug delivery to the target region. The SASA analysis introduced BCN nanosheet as the best system for targeted drug delivery.

Investigation of van der Waals (vdW) and electrostatic bonds between drug and nano-carrier by using energy analysis:

Chemical bonds hold molecules together temporarily or permanently. As intermolecular bonds are weaker than bonds between the and most well-known of these bonds are vdW and electrostatic bonds, vdW bonds arise from the induction of an electric field from one atom's instantaneous dipoles to another and are known as vdW forces. At long distances (in nanometers), these forces attract and repel at close distances. Electrostatic bonds are formed due to the presence of opposite charges. The force between two atoms follows Coulomb's law with opposite charges. Successful drug delivery to the target region requires strong drug-Nano-carrier bonds. Energy analysis is one of the most fundamental indicators for comparing intermolecular interaction. By the energy analysis, it is possible to calculate the electrostatic and vdW forces' contributions in the intermolecular interactions. The stronger the intermolecular bonds, the greater the absolute value of the simulation energy [63–66]. Polymeric micelles and carbon nanoparticles were considered as Nano-carrier. The sum of the average energy from electrostatic and vdW bonds was considered the investigation criterion to investigate the strength of drug-Nano-carrier bonds. In this study, mmpbsa[67,68]software was utilized to calculate the energy contribution of electrostatic and vdW bonds.

Table 13 shows the average electrostatic and vdW energy in BCN Fullerene, Fullerene, N doped Fullerene, and P doped Fullerene systems. The BCN Fullerene system illuminates the highest absolute value of electrostatic energy (369, 4648) followed by Fullerene, P doped Fullerene, and N doped Fullerene, respectively. Furthermore, the highest absolute magnitude of vdW energy was found in the BCN Fullerene system (750, 7997), followed by P doped Fullerene, Fullerene, and N doped Fullerene, respectively. Figure 8 shows the portion of drug-polymer micelles energy and the one between the drug and Fullerenes. The drug-polymer micelles energy predominated the total energy in all simulations. The drug-polymer micelles interaction was much stronger than the interactions between the drug and Fullerenes. BCN Fullerene showed the highest sum of vdW and electrostatics energy. Consequently, P doped Fullerene, Fullerene, and N doped Fullerene take the next places in this regard. The higher absolute value of vdW and electrostatic energy in the BCN Fullerene system indicates stronger drug-Nano-carrier interactions that prevent drug release to unwanted sites. Among the simulated Fullerenes, BCN Fullerene provided the best conditions for targeted drug delivery.

Table 14 shows the average electrostatic and vdW energies in BCN nanosheet, Graphene, N doped Graphene, and P doped Graphene systems. The P doped Graphene system showed the highest absolute value of electrostatic energy (632.12346), followed by the N doped Graphene, BCN nanosheet, and Graphene, respectively. The higher electrostatic energy in the P doped Graphene simulation implies the more vigorous the electrostatic bonds between the nano-carrier and the drug. The BCN nanosheet offered the highest absolute vdW energy (1100.595), followed by P doped Graphene, N doped Graphene, and

Graphene, respectively. The greater absolute value of vdW energy in the BCN nanosheet system indicates the stronger vdW bonds between the carrier and the drug. Figure 9 shows the drug-polymer micelles energy portion and drug- nanosheet energy. In the P doped Graphene, the drug-polymer micelles energy did not significantly differ with the energy between the drug and the P doped Graphene. However, the drug-polymer micelles energy dominated in the other three simulations in Fig. 9. The total absolute value of vdW and electrostatic energies in the BCN nanosheet simulation was the highest, followed by the P doped Graphene, N doped Graphene, and Graphene simulations, respectively. The greater the absolute total energy in the BCN nanosheet system means stronger interactions between the drug and the polymer-carrying nanomaterial which prevents the drug release in the unwanted sites. Among the simulated nanosheet, BCN nanosheet provided the best conditions for targeted drug delivery.

Table 15 shows the average electrostatic and vdW energy in the BCN nanotube, CNT, N doped nanotube, and P doped nanotube. The BCN nanotube showed the highest absolute electrostatic energy (370.32 followed by CNT, P doped nanotube, and N doped nanotube, respectively. The greater electrostatic energy in BCN nanotube implies stronger electrostatic bonds between the nano-carrier and the drug. The BCN nanotube also offered the highest absolute vdW energy (788.7657), followed by N doped nanotube, CNT, and P doped nanotube, respectively. The higher value of vdW energy in BCN nanotube simulation indicates the stronger vdW bonds between the Nano-carrier and drug. Figure 10 shows the contributions of drug-polymer micelle and drug- CNT energies to the total energy. The drug-polymer micelle energy predominated the total energy, suggesting that the drug-polymer micelle interactions are much stronger than the drug-nanotube interactions. It had the highest value in BCN nanotube simulation. After BCN nanotube, the absolute total energy was the highest in the CNT, P doped nanotube, and N doped nanotube systems, respectively. The higher absolute value of total energy in the BCN nanotube simulation indicates stronger drug-Nano-carrier interactions, preventing the drug release in the unwanted sites. Among the simulated CNTs, BCN nanotube provided the best conditions for targeted drug delivery. The sum of absolute vdW and electrostatic energies was 1480.815, 1159.0857, and 1120.2646 for BCN nanosheet, BCN nanotube, and BCN Fullerene, respectively. As can be seen, the BCN nanosheet possessed the highest absolute total energy implying the most potent drug-Nano-carrier interactions, preventing the drug release in unwanted parts of the body and thus better drug transfer. The energy analysis introduced BCN nanosheet as the best nanoparticle for targeted drug delivery purposes.

Conclusion

The proper transfer of the drug to the cancer cells is of great importance in cancer treatment. Among different nano-carriers have been used to transfer the drug to the cancer cells. In this paper we examined various types of Fullerenes, nanosheets, and CNTs for drug transfer to cancer cells using MD simulations. We performed Rg, H-bond, RDF, SASA, and energy analyses for all systems. BCN Fullerene exhibited the largest reduction in the Rg. Thus, BCN Fullerene could be the best nanoparticle for drug transfer among the studied Fullerenes. This system also offered the highest maximum RDF, the lowest contact area, the highest number of H-bonds, and the largest drug adsorption energy. The results of energy, H-bond, RDF, and SASA analyses confirmed the result of Rg analysis. BCN nanosheet was introduced as the best

nanosheet for drug transfer. It had the most considerable reduction in Rg, the highest maximum RDF, the lowest drug contact area, and the highest average number of H-bonds as well as the most significant drug adsorption energy. The results of energy, H-bond, RDF, and SASA analyses were in line with the Rg analysis findings. BCN nanotube system exhibited the largest reduction in Rg. The BCN nanotube was selected as the best nanotube for drug transfer as it possessed the highest maximum RDF, the lowest drug contact, the largest average number of H-bonds, and the highest drug adsorption energy. The results of energy, H-bond, RDF, and SASA analysis confirmed the result of Rg analysis. In the studied categories, BCN Fullerene, BCN nanosheet, and BCN nanotube created the best drug delivery conditions for the target site, respectively. BCN nanosheet simulation showed the largest reduction in Rg, the largest maximum RDF, the lowest drug contact, the highest average number of H-bonds, and the highest drug adsorption energy. Therefore, BCN nanosheet is the best nanoparticle for drug delivery to the target area. It is also recommended to assess the transfer of DOX by a BCN nanosheet nanoparticle under laboratory conditions to investigate BCN effect of nanosheet over long periods of time.

Abbreviations

MD	Molecular Dynamics
PLGA	Poly Lactic-co-Glycolic Acid
PEG	Polyethylene Glycol
DOX	Doxorubicin
RDF	Radial Distribution Function
H-Bond	Hydrogen Bonds
vdW	van der Waals
Rg	Radius of gyration
SASA	Solvent Accessible Surface Area
BCN	Boron Carbon Nitride
P doped	Phosphorus doped
N doped	Nitrogen doped
CNT	Carbon Nano Tube
DDS	Drug delivery systems
DLS	Dynamic Light Scattering
EMA	European Medicines Agency
FDA	Food and Drug Administration

References

1. Torre LA, Siegel RL, Islami F, Bray F, Jemal A. Worldwide Burden of and Trends in Mortality From Gallbladder and Other Biliary Tract Cancers. Clin Gastroenterol Hepatol. 2018;16(3):427-437. doi:10.1016/j.cgh.2017.08.017
2. Djema W, Bonnet C, Mazenc F, et al. Control in dormancy or eradication of cancer stem cells: Mathematical modeling and stability issues. J Theor Biol. 2018;449:103-123. doi:10.1016/j.jtbi.2018.03.038
3. Levine AJ, Jenkins NA, Copeland NG. The Roles of Initiating Truncal Mutations in Human Cancers: The Order of Mutations and Tumor Cell Type Matters. Cancer Cell. 2019;35(1):10-15. doi:10.1016/j.ccell.2018.11.009
4. Khan J, Alexander A, Ajazuddin, Saraf S, Saraf S. Exploring the role of polymeric conjugates toward anti-cancer drug delivery: Current trends and future projections. Int J Pharm. 2018;548(1):500-514. doi:10.1016/j.ijpharm.2018.06.060
5. Fonseca TG, Auguste M, Ribeiro F, et al. Environmental relevant levels of the cytotoxic drug cyclophosphamide produce harmful effects in the polychaete Nereis diversicolor. Sci Total Environ. 2018;636:798-809. doi:10.1016/j.scitotenv.2018.04.318
6. Tripathi PK, Tripathi S. Dendrimers for Anticancer Drug Delivery. Elsevier Inc.; 2020. doi:10.1016/b978-0-12-814527-2.00006-8
7. Sharma P, Mehta M, Dhanjal DS, et al. Emerging trends in the novel drug delivery approaches for the treatment of lung cancer. Chem Biol Interact. 2019;309(June):108720. doi:10.1016/j.cbi.2019.06.033
8. Mishra DK, Yadav KS, Prabhakar B, Gaud RS. Nanocomposite for Cancer Targeted Drug Delivery. Elsevier Inc.; 2018. doi:10.1016/B978-0-12-813741-3.00014-5
9. Santos LF, Correia IJ, Silva AS, Mano JF. Biomaterials for drug delivery patches. Eur J Pharm Sci. 2018;118(March):49-66. doi:10.1016/j.ejps.2018.03.020
10. Rotman SG, Grijpma DW, Richards RG, Moriarty TF, Eglin D, Guillaume O. Drug delivery systems functionalized with bone mineral seeking agents for bone targeted therapeutics. J Control Release. 2018;269:88-99. doi:10.1016/j.jconrel.2017.11.009
11. Zamani M, Naderi E, Aghajanzadeh M, Naseri M, Sharafi A, Danafar H. Co1−XZnxFe2O4 based Nano-carriers for dual-targeted anticancer drug delivery: Synthesis, characterization and in vivo and in vitro biocompatibility study. J Mol Liq. 2019;274:60-67. doi:10.1016/j.molliq.2018.10.083
12. Chen X, Tong R, Shi Z, et al. MOF Nanoparticles with Encapsulated Autophagy Inhibitor in Controlled Drug Delivery System for Antitumor. ACS Appl Mater Interfaces. 2018;10(3):2328-2337. doi:10.1021/acsami.7b16522
13. Kröger APP, Paulusse JMJ. Single-chain polymer nanoparticles in controlled drug delivery and targeted imaging. J Control Release. 2018;286(July):326-347. doi:10.1016/j.jconrel.2018.07.041
14. Qiu L, Zhao L, Xing C, Zhan Y. Redox-responsive polymer prodrug/AgNPs hybrid nanoparticles for drug delivery. Chinese Chem Lett. 2018;29(2):301-304. doi:10.1016/j.cclet.2017.09.048

15. Zhou Y, Quan G, Wu Q, et al. Mesoporous silica nanoparticles for drug and gene delivery. Acta Pharm Sin B. 2018;8(2):165-177. doi:10.1016/j.apsb.2018.01.007
16. Rizvi SAA, Saleh AM. Applications of nanoparticle systems in drug delivery technology. Saudi Pharm J. 2018;26(1):64-70. doi:10.1016/j.jsps.2017.10.012
17. Mahajan S, Patharkar A, Kuche K, et al. Functionalized CNTs as emerging delivery system for the treatment of cancer. Int J Pharm. 2018;548(1):540-558. doi:10.1016/j.ijpharm.2018.07.027
18. Pan Y, Sun K, Liu S, et al. Core-Shell ZIF-8@ZIF-67-Derived CoP Nanoparticle-Embedded N-Doped CNT Hollow Polyhedron for Efficient Overall Water Splitting. J Am Chem Soc. 2018;140(7):2610-2618. doi:10.1021/jacs.7b12420
19. Karthika V, Kaleeswarran P, Gopinath K, et al. Biocompatible properties of nano-drug carriers using TiO2-Au embedded on multiwall CNTs for targeted drug delivery. Mater Sci Eng C. 2018;90(2017):589-601. doi:10.1016/j.msec.2018.04.094
20. Al-Qattan MN, Deb PK, Tekade RK. Molecular dynamics simulation strategies for designing carbon-nanotube-based targeted drug delivery. Drug Discov Today. 2018;23(2):235-250. doi:10.1016/j.drudis.2017.10.002
21. Raphey VR, Henna TK, Nivitha KP, Mufeedha P, Sabu C, Pramod K. Advanced biomedical applications of CNT. Mater Sci Eng C. 2019;100(February):616-630. doi:10.1016/j.msec.2019.03.043
22. Samrot A V., Burman U, Philip SA, Shobana N, Chandrasekaran K. Synthesis of curcumin loaded polymeric nanoparticles from crab shell derived chitosan for drug delivery. Informatics Med Unlocked. 2018;10:159-182. doi:10.1016/j.imu.2017.12.010
23. Wang C, Wang Z, Zhao X, et al. DOX Loaded Aggregation-induced Emission Active Polymeric Nanoparticles as a Fluorescence Resonance Energy Transfer Traceable Drug Delivery System for Self-indicating Cancer Therapy. Acta Biomater. 2019;85:218-228. doi:10.1016/j.actbio.2018.12.020
24. Gao W, Chen Y, Zhang Y, Zhang Q, Zhang L. Nanoparticle-based local antimicrobial drug delivery. Adv Drug Deliv Rev. 2018;127:46-57. doi:10.1016/j.addr.2017.09.015
25. George A, Shah PA, Shrivastav PS. Natural biodegradable polymers based nano-formulations for drug delivery: A review. Int J Pharm. 2019;561(March):244-264. doi:10.1016/j.ijpharm.2019.03.011
26. Sharma S, Parmar A, Kori S, Sandhir R. PLGA-based nanoparticles: A new paradigm in biomedical applications. TrAC - Trends Anal Chem. 2016;80(December):30-40. doi:10.1016/j.trac.2015.06.014
27. Swider E, Koshkina O, Tel J, Cruz LJ, de Vries IJM, Srinivas M. Customizing poly(lactic-co-glycolic acid) particles for biomedical applications. Acta Biomater. 2018;73:38-51. doi:10.1016/j.actbio.2018.04.006
28. Li X, Jiang X. Microfluidics for producing poly (lactic-co-glycolic acid)-based pharmaceutical nanoparticles. Adv Drug Deliv Rev. 2018;128:101-114. doi:10.1016/j.addr.2017.12.015
29. Deb A, Vimala R. Camptothecin loaded graphene oxide nanoparticle functionalized with polyethylene glycol and folic acid for anticancer drug delivery. J Drug Deliv Sci Technol. 2018;43(April 2017):333-342. doi:10.1016/j.jddst.2017.10.025

30. Poudel AJ, He F, Huang L, Xiao L, Yang G. Supramolecular hydrogels based on poly (ethylene glycol)-poly (lactic acid) block copolymer micelles and α-cyclodextrin for potential injectable drug delivery system. Carbohydr Polym. 2018;194:69-79. doi:10.1016/j.carbpol.2018.04.035
31. Duan X, Bai T, Du J, Kong J. One-pot synthesis of glutathione-responsive amphiphilic drug self-delivery micelles of doxorubicin-disulfide-methoxy polyethylene glycol for tumor therapy. J Mater Chem B. 2017;6(1):39-43. doi:10.1039/c7tb02817b
32. Saedisomeolia A, Ashoori M. Riboflavin in Human Health: A Review of Current Evidences. Vol 83. 1st ed. Elsevier Inc.; 2018. doi:10.1016/bs.afnr.2017.11.002
33. Heimer G, Eyal E, Zhu X, et al. Mutations in AIFM1 cause an X-linked childhood cerebellar ataxia partially responsive to riboflavin. Eur J Paediatr Neurol. 2018;22(1):93-101. doi:10.1016/j.ejpn.2017.09.004
34. González-Santamaría R, Ruiz-González R, Nonell S, Garde-Cerdán T, Pérez-Álvarez EP. Influence of foliar riboflavin applications to vineyard on grape amino acid content. Food Chem. 2018;240:601-606. doi:10.1016/j.foodchem.2017.07.115
35. Sima Rezvantalab, a Mostafa Keshavarz Moraveji a MK a and RM b. An Insight into The Role of Riboflavin Ligand on the Self-assembly of Poly (lactic-co-glycolic acid)-based Nanoparticles, A Molecular Simulation and Experimental Approach. Soft Matter. Published online 2020. doi:10.1002/9783527682300
36. Mortazavifar A, Raissi H, Akbari A. DFT and MD investigations on the functionalized boron nitride nanotube as an effective drug delivery carrier for Carmustine anticancer drug. J Mol Liq. 2019;276:577-587. doi:10.1016/j.molliq.2018.12.028
37. Shafiei F, Hashemianzadeh SM, Bagheri Y. Insight into the encapsulation of gemcitabine into boron-nitride nanotubes and gold cluster triggered release: A molecular dynamics simulation. J Mol Liq. 2019;278:201-212. doi:10.1016/j.molliq.2019.01.020
38. Wang L, Xu J, Wang X, Cheng Z, Xu J. Facile preparation of N-rich functional polymer with porous framework as QCM sensing material for rapid humidity detection. Sensors Actuators, B Chem. 2019;288(February):289-297. doi:10.1016/j.snb.2019.02.058
39. Chen W, He J, Jiang Y, Zhang H, Zhou X. Experimental and theoretical studies on the atmospheric degradation of 1, 1, 2, 2, 3, 3, 4-heptafluorocyclopentane. Atmos Environ. 2019;196:38-43. doi:10.1016/j.atmosenv.2018.09.057
40. Robertson MJ, Qian Y, Robinson MC, Tirado-Rives J, Jorgensen WL. Development and Testing of the OPLS-AA/M Force Field for RNA. J Chem Theory Comput. 2019;15(4):2734-2742. doi:10.1021/acs.jctc.9b00054
41. Dalgicdir C, Van Der Vegt NFA. Improved Temperature Behavior of PNIPAM in Water with a Modified OPLS Model. J Phys Chem B. 2019;123(17):3875-3883. doi:10.1021/acs.jpcb.9b01644
42. Itliong JN, Villagracia ARC, Moreno JL V., et al. Investigation of reverse ionic diffusion in forward-osmosis-aided dewatering of microalgae: A molecular dynamics study. Bioresour Technol. 2019;279(January):181-188. doi:10.1016/j.biortech.2019.01.109

43. Kyrychenko A, Blazhynska MM, Slavgorodska M V., Kalugin ON. Stimuli-responsive adsorption of poly(acrylic acid) onto silver nanoparticles: Role of polymer chain length and degree of ionization. J Mol Liq. 2019;276:243-254. doi:10.1016/j.molliq.2018.11.130
44. Herrera-Rodríguez AM, Miletić V, Aponte-Santamaría C, Gräter F. Molecular Dynamics Simulations of Molecules in Uniform Flow. Biophys J. 2019;116(9):1579-1585. doi:10.1016/j.bpj.2018.12.025
45. Zhong W, Cai Y, Tománek D. Computer simulation of hydrogen embrittlement in metals. Nature. 1993;362(6419):435-437. doi:10.1038/362435a0
46. Martoňák R, Donadio D, Oganov AR, Parrinello M. Crystal structure transformations in SiO2 from classical and ab initio metadynamics. Nat Mater. 2006;5(8):623-626. doi:10.1038/nmat1696
47. Carretero-González R, Kevrekidis PG, Kevrekidis IG, Maroudas D, Frantzeskakis DJ. A Parrinello-Rahman approach to vortex lattices. Phys Lett Sect A Gen At Solid State Phys. 2005;341(1-4):128-134. doi:10.1016/j.physleta.2005.04.046
48. Kharazian B, Lohse SE, Ghasemi F, et al. Bare surface of gold nanoparticle induces inflammation through unfolding of plasma fibrinogen. Sci Rep. 2018;8(1):1-9. doi:10.1038/s41598-018-30915-7
49. Maleki R, Afrouzi HH, Hosseini M, Toghraie D, Rostami S. Molecular dynamics simulation of Doxorubicin loading with N-isopropyl acrylamide CNT in a drug delivery system. Comput Methods Programs Biomed. 2020;184:105303. doi:10.1016/j.cmpb.2019.105303
50. Ajori S, Ansari R, Haghighi S. A molecular dynamics study on the buckling behavior of cross-linked functionalized CNTs under physical adsorption of polymer chains. Appl Surf Sci. 2018;427:704-714. doi:10.1016/j.apsusc.2017.08.049
51. Shariatinia Z, Mazloom-Jalali A. Chitosan nanocomposite drug delivery systems designed for the ifosfamide anticancer drug using molecular dynamics simulations. J Mol Liq. 2019;273:346-367. doi:10.1016/j.molliq.2018.10.047
52. Xu WS, Carrillo JMY, Lam CN, Sumpter BG, Wang Y. Molecular Dynamics Investigation of the Relaxation Mechanism of Entangled Polymers after a Large Step Deformation. ACS Macro Lett. 2018;7(2):190-195. doi:10.1021/acsmacrolett.7b00900
53. Fang H, Tang Z, Liu X, Huang Y, Sun CQ. Discriminative ionic capabilities on hydrogen-bond transition from the mode of ordinary water to (Mg, Ca, Sr)(Cl, Br) 2 hydration. J Mol Liq. 2019;279:485-491. doi:10.1016/j.molliq.2019.01.147
54. Zhong Y, Chen Y, Feng X, et al. Hydrogen-bond facilitated intramolecular proton transfer in excited state and fluorescence quenching mechanism of flavonoid compounds in aqueous solution. J Mol Liq. 2020;302:112562. doi:10.1016/j.molliq.2020.112562
55. Bu R, Xiong Y, Wei X, Li H, Zhang C. Hydrogen Bonding in CHON-Containing Energetic Crystals: A Review. Cryst Growth Des. 2019;19(10):5981-5997. doi:10.1021/acs.cgd.9b00853
56. Zhang Q, Han Y, Wu L. Influence of electrostatic field on the adsorption of phenol on single-walled CNTs: A study by molecular dynamics simulation. Chem Eng J. 2019;363(December 2018):278-284. doi:10.1016/j.cej.2019.01.146

57. Han Y, Zhu L, Zhang Y. Molecular dynamics simulation for the impact of external electric fields on CaCl2 aqueous solution. Chem Res Chinese Univ. 2016;32(4):641-646. doi:10.1007/s40242-016-6106-6
58. Dahal U, Adhikari NP. Molecular dynamics study of diffusion of heavy water in normal water at different temperatures. J Mol Liq. 2012;167:34-39. doi:10.1016/j.molliq.2011.12.008
59. de Oliveira OV, Costa LT, Leite ER. Molecular modeling of a polymer nanocomposite model in water and chloroform solvents. Comput Theor Chem. 2016;1092:52-56. doi:10.1016/j.comptc.2016.08.005
60. Pires JM, de Oliveira O V., Freitas LCG, Filho EA d. S, Prado AR. Molecular dynamic simulations of polyacrylonitrile in ethanol and water solvents. Comput Theor Chem. 2012;995:75-78. doi:10.1016/j.comptc.2012.06.032
61. Poudyal I, Adhikari NP. Temperature dependence of diffusion coefficient of carbon monoxide in water: A molecular dynamics study. J Mol Liq. 2014;194:77-84. doi:10.1016/j.molliq.2014.01.004
62. Uddin M, Coombe D, Ivory J. Molecular dynamics analysis of compositional effects in hydrocarbon systems property calculations. Chem Eng J. 2016;302:503-515. doi:10.1016/j.cej.2016.05.080
63. Astrand P, Wallqvist A, Karlström G. Intermolecular interactions of urea and water. J Chim Phys. 1991;88:2457-2464. doi:10.1051/jcp/1991882457
64. Damghani T, Sedghamiz T, Sharifi S, Pirhadi S. Critical c-Met-inhibitor interactions resolved from molecular dynamics simulations of different c-Met complexes. J Mol Struct. 2020;1203:127456. doi:10.1016/j.molstruc.2019.127456
65. Dehury B, Behera SK, Mahapatra N. Structural dynamics of Casein Kinase I (CKI) from malarial parasite Plasmodium falciparum (Isolate 3D7): Insights from theoretical modelling and molecular simulations. J Mol Graph Model. 2017;71:154-166. doi:10.1016/j.jmgm.2016.11.012
66. Maleki R, Afrouzi HH, Hosseini M, Toghraie D, Piranfar A, Rostami S. pH-sensitive loading/releasing of doxorubicin using single-walled CNT and multi-walled CNT: A molecular dynamics study. Comput Methods Programs Biomed. 2020;186:105210. doi:10.1016/j.cmpb.2019.105210
67. Wang E, Sun H, Wang J, et al. End-Point Binding Free Energy Calculation with MM/PBSA and MM/GBSA: Strategies and Applications in Drug Design. Chem Rev. 2019;119(16):9478-9508. doi:10.1021/acs.chemrev.9b00055
68. Greene D, Qi R, Nguyen R, Qiu T, Luo R. Heterogeneous Dielectric Implicit Membrane Model for the Calculation of MMPBSA Binding Free Energies. J Chem Inf Model. 2019;59(6):3041-3056. doi:10.1021/acs.jcim.9b00363

Tables

Table 1. Differences between the initial and final Rg in different types of Fullerenes.

	BCN Fullerene	Fullerene	N doped Fullerene	P doped Fullerene
Rg0-Rg100	1.16263	-0.73552	0.33926	0.9833

Table 2. The difference between the initial and final Rg in different types of Nanosheets.

	BCN Nanosheet	Graphene	N doped Graphene	P doped Graphene
Rg0-Rg100	1.40905	0.59461	1.03089	1.27934

Table 3. The difference between the initial and final Rg in different types of nanotubes.

	BCN Nanotube	CNT	N doped Nanotube	P doped Nanotube
Rg0-Rg100	1.17895	0.91054	-0.24661	-0.18114

Table 4. Average number of H-Bonds formed between drug and polymer micelles in Fullerenes.

	BCN Fullerene	Fullerene	N doped Fullerene	P doped Fullerene
Average of Hydrogen bonds	2.207	2.058	2.122	2.152

Table 5. Average number of H-Bonds formed between drug and polymer micelles in Nanosheets.

	BCN Nanosheet	Graphene	N doped Graphene	P doped Graphene
Average of Hydrogen bonds	3.972	3.867	2.697	3.901

Table 6. Average number of H-Bonds formed between drug and polymer micelles in CNTs.

	BCN Nanotube	CNT	N doped Nanotube	P doped Nanotube
Average of Hydrogen bonds	2.630	2.342	2.243	2.089

Table 7. Maximum RDF values of different types of Fullerenes.

	BCN Fullerene	Fullerene	N doped Fullerene	P doped Fullerene
Maximum of RDF value	3.701	3.588	2.864	3.654

Table 8. Maximum RDF values of various types of nanosheet.

	BCN Nanosheet	Graphene	N doped Graphene	P doped Graphene
Maximum of RDF value	3.876	3.042	2.859	3.246

Table 9. Maximum RDF values of CNTs.

	BCN Nanotube	CNT	N doped Nanotube	P doped Nanotube
Maximum of RDF value	3.781	3.576	3.449	3.093

Table 10. Average drug contact area for different types of Fullerenes.

	BCN Fullerene	Fullerene	N doped Fullerene	P doped Fullerene
Average of Contact Area	217.739	225.833	219.067	218.193

Table 11. Average drug contact area for different types of nanosheet.

	BCN Nanosheet	Graphene	N doped Graphene	P doped Graphene
Average of Contact Area	214.6429973	224.4924712	227.6131757	220.9176829

Table 12. Average drug contact area for different types of CNTs.

	BCN Nanotube	CNT	N doped Nanotube	P doped Nanotube
Average of Contact Area	216.7167637	219.0642917	224.5664497	229.810576

Table 13. Average energy of different types of Fullerenes over 100 ns.

	BCN Fullerene	Fullerene	N doped Fullerene	P doped Fullerene
vdW (kJ/mol)	-750.7997904	-631.3899747	-525.8328156	-613.040569
Electrostatic (kJ/mol)	-369.464899	-314.75	-333.284189	-354.3081917
Total energy (kJ/mol)	-1120.264689	-946.1399716	-859.1170046	-967.3487607

Table 14. Average energy of different nanosheets over 100 ns.

	BCN Nanosheet	Graphene	N doped Graphene	P doped Graphene
vdW (kJ/mol)	-1100.59511	-562.5363706	-742.367553	-799.5848747
Electrostatic (kJ/mol)	-380.22	-350.0769	-389.9860683	-632.1234696
Total energy (kJ/mol)	-1480.81511	-912.6133	-1132.353621	-1431.708344

Table 15. Average energy of different nanotubes over 100 ns.

	BCN Nanotube	CNT	N doped Nanotube	P doped Nanotube
vdW (kJ/mol)	-788.7657532	-753.3847825	-765.419484	-747.7290748
Electrostatic (kJ/mol)	-370.32	-330.67	-267.6899891	-286.6715174
Total energy (kJ/mol)	-1159.085753	-1084.054783	-1033.109473	-1034.400592

Figures

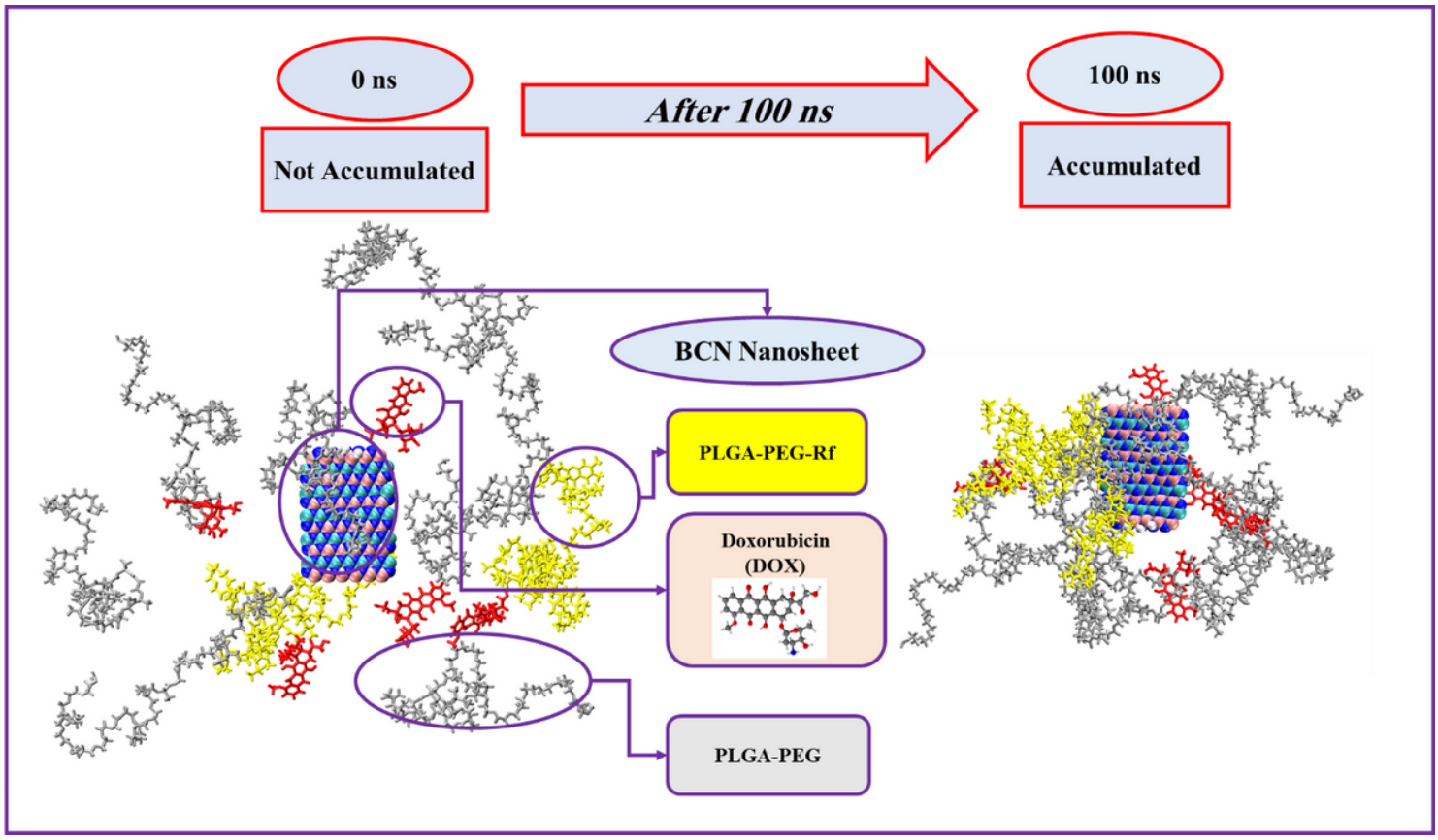

Figure 1

Accumulation of polymer particles by reducing the Rg.

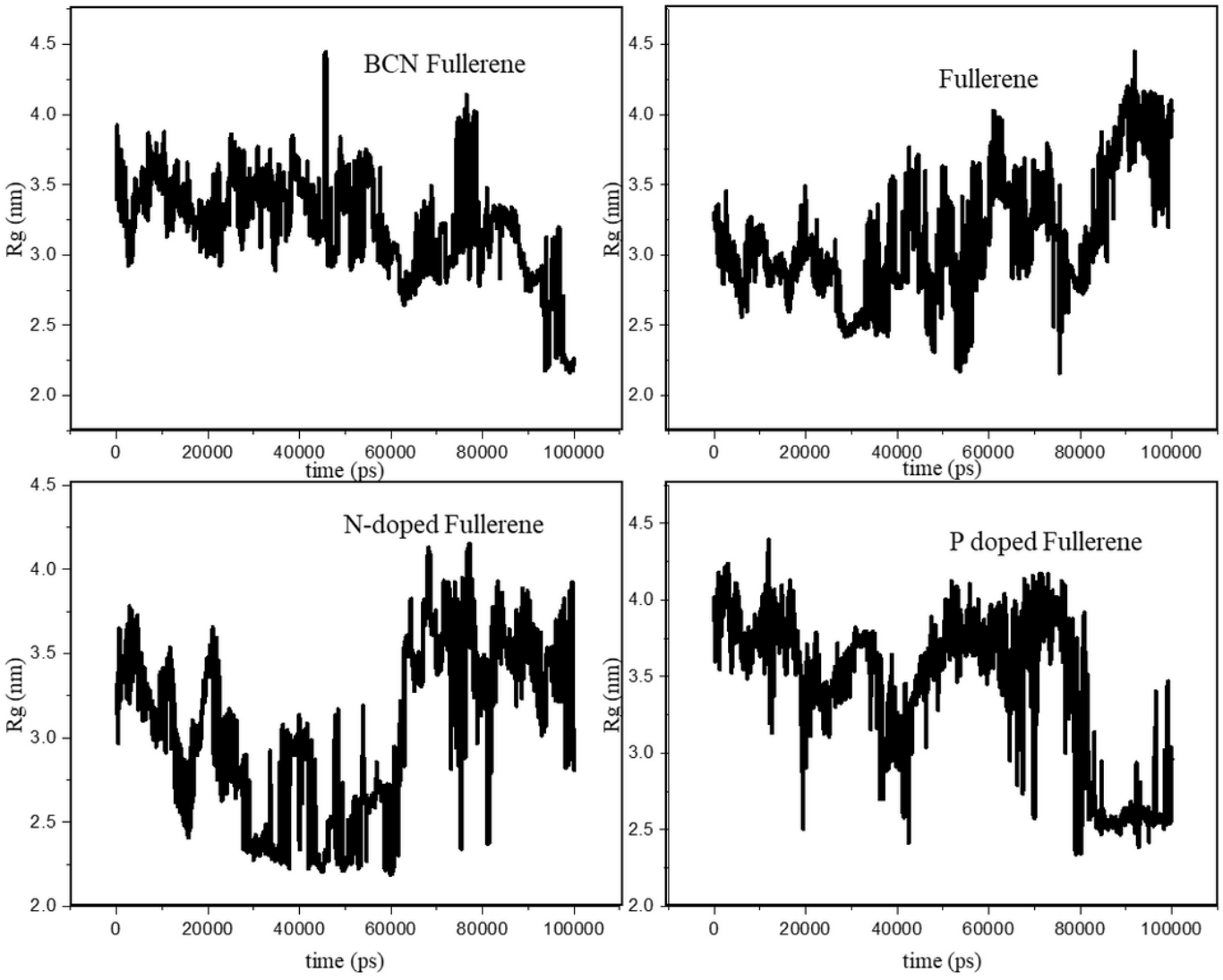

Figure 2

Rg diagram of Fullerenes over 100 nm.

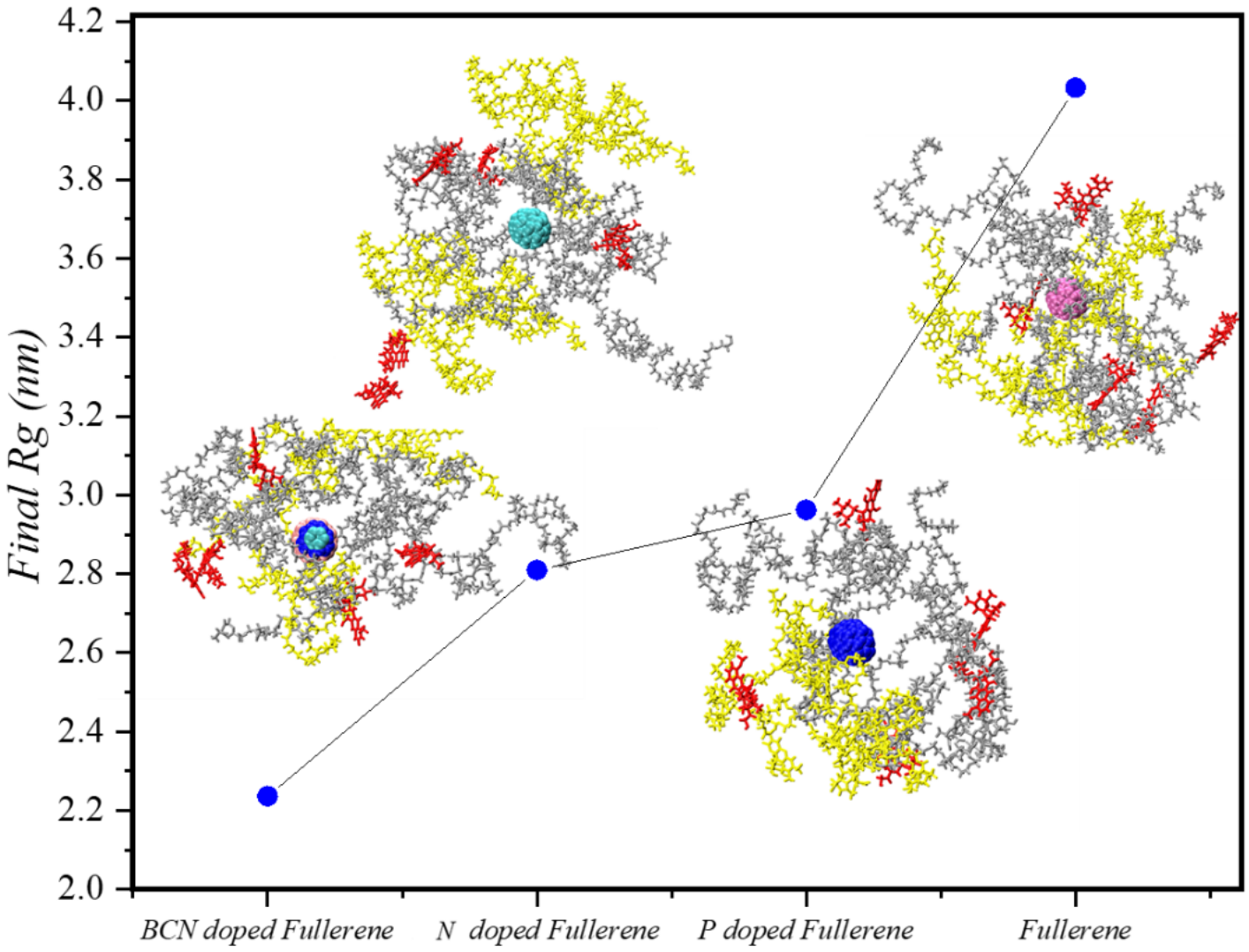

Figure 3

The final Rg values of different types of Fullerene systems.

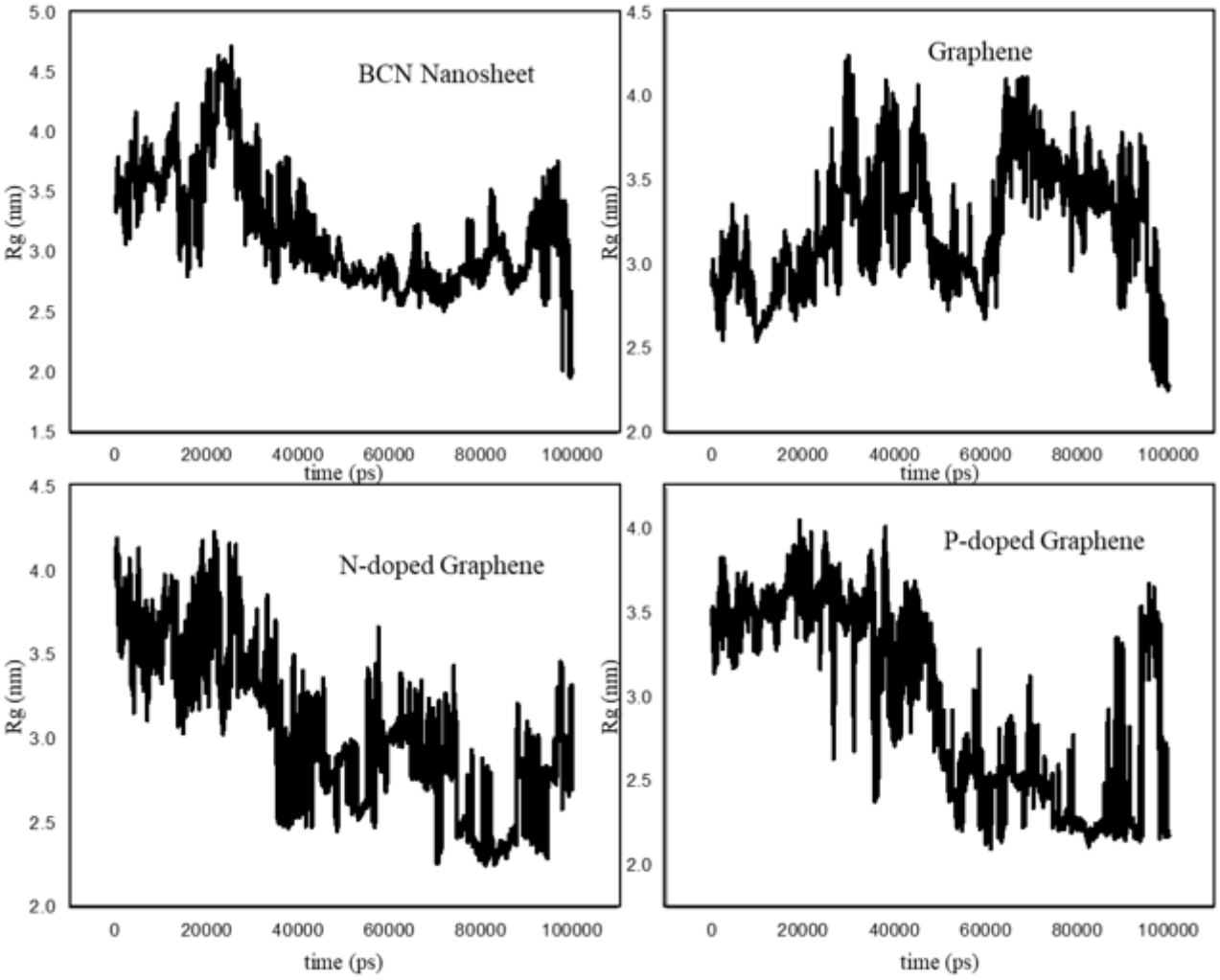

Figure 4

Rg diagram of Nanosheets over 100 ns.

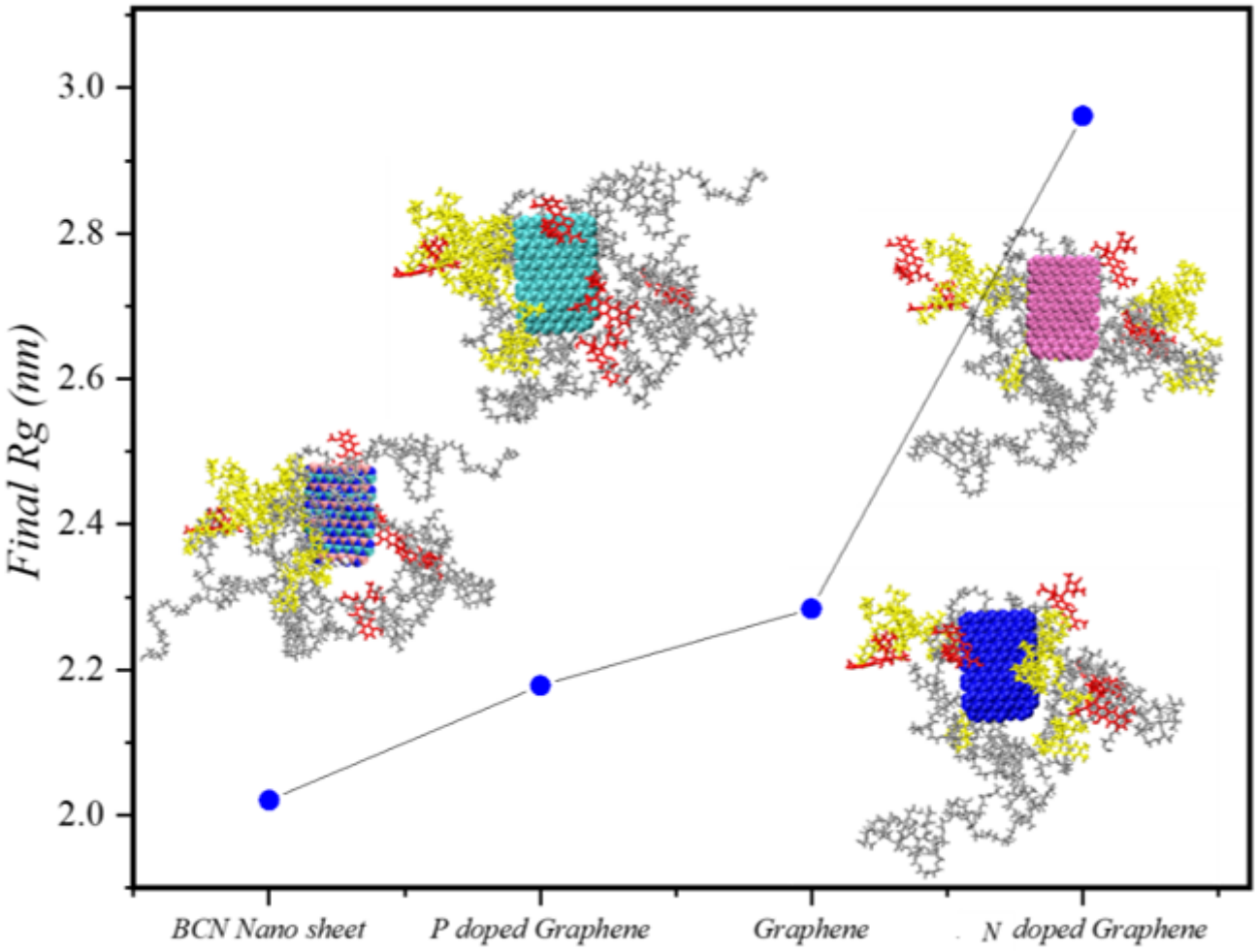

Figure 5

The final Rg values of different types of Nanosheets.

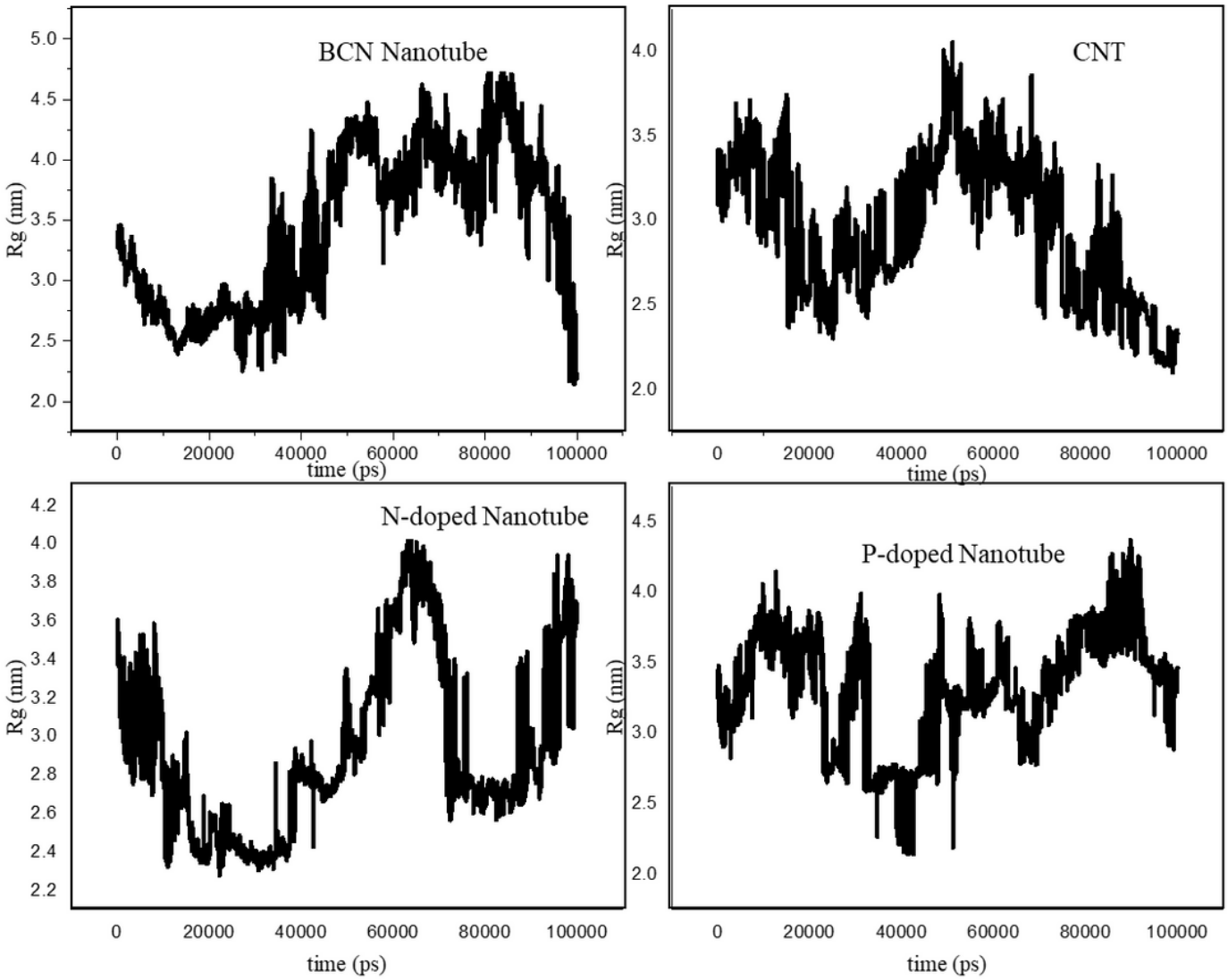

Figure 6

Rg diagram of CNTs over 100 ns.

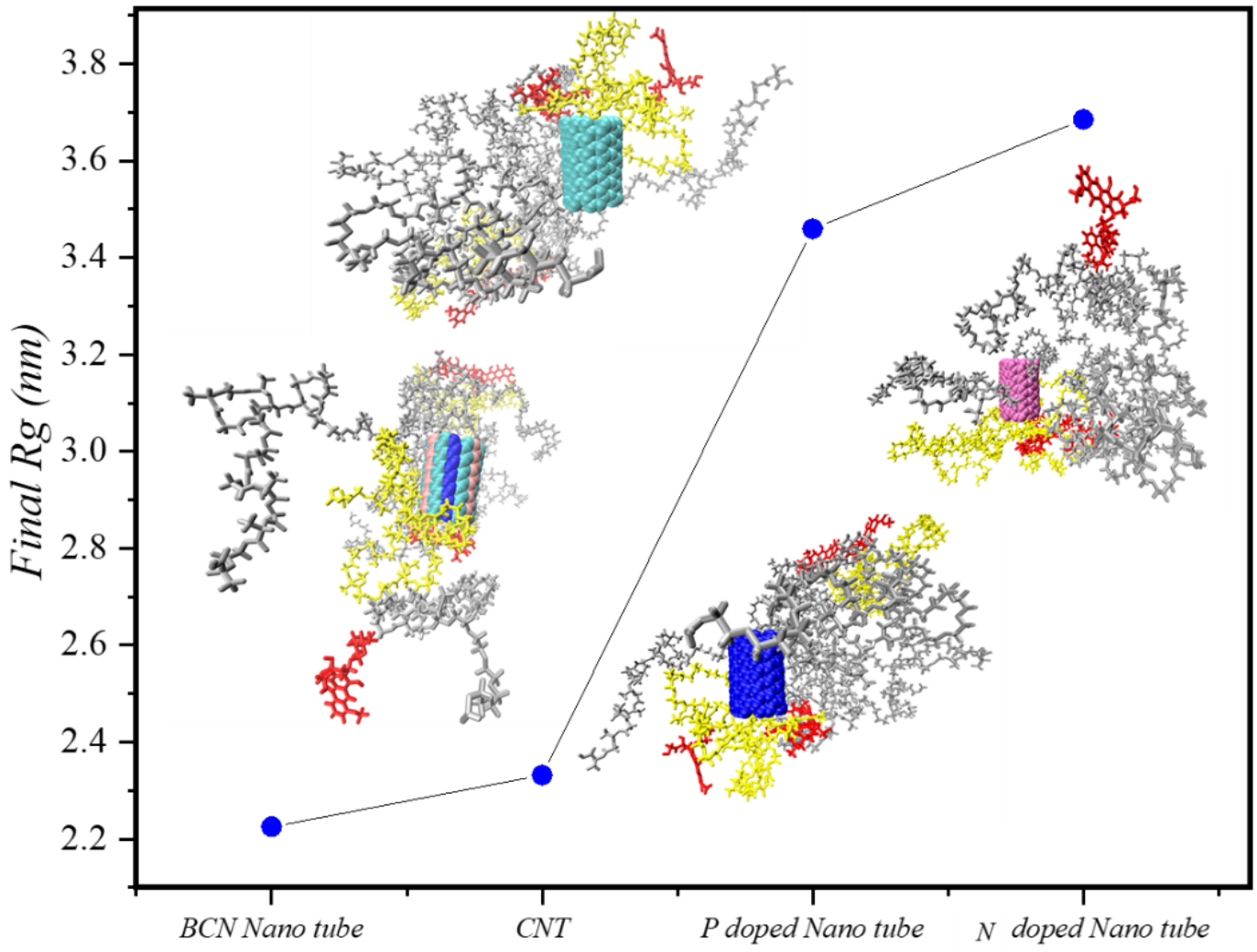

Figure 7

Final Rg of different types of CNTs.

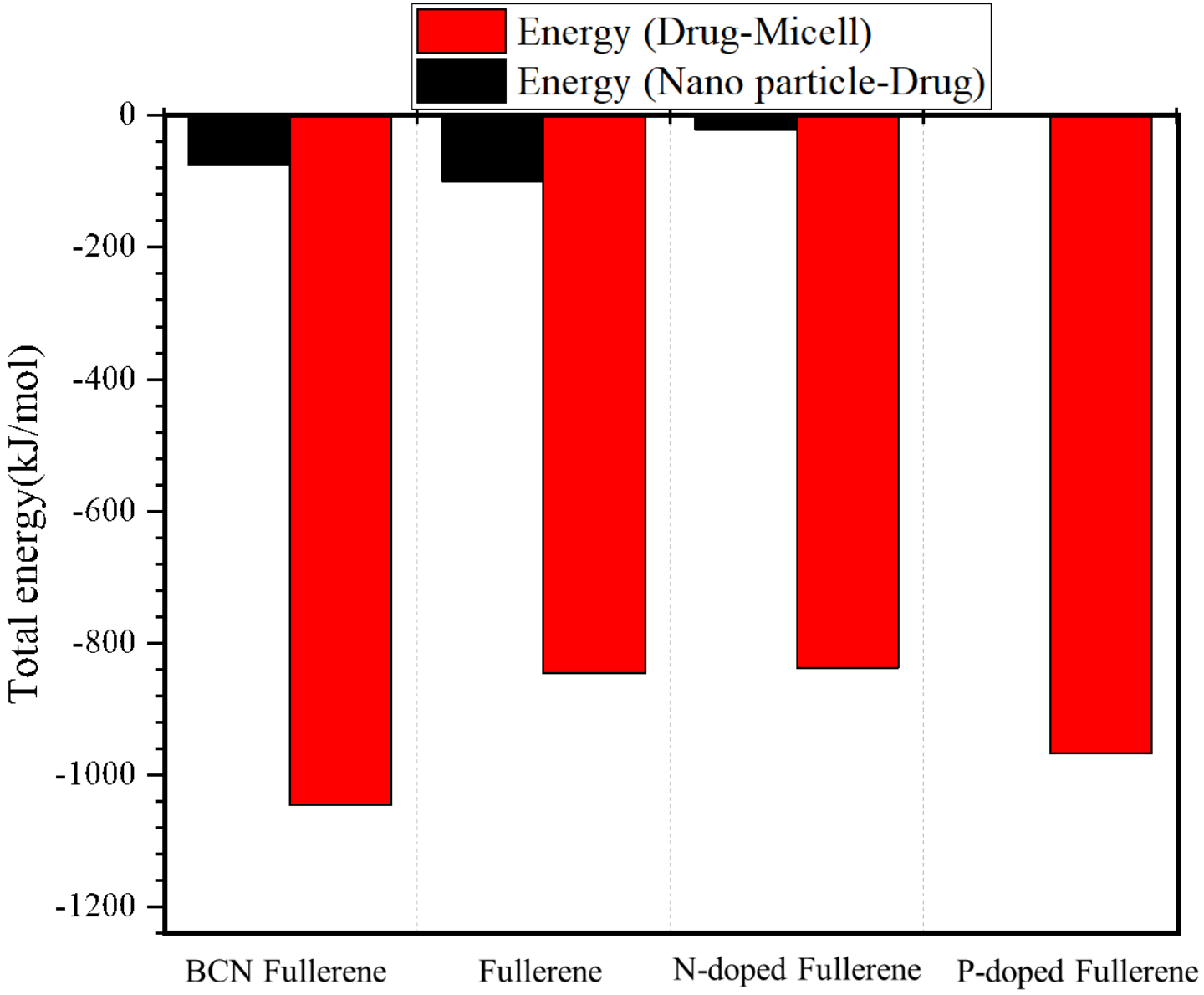

Figure 8

The contribution of vdW and electrostatic energies in the average drug-polymer micelles energy and the average drug-Fullerenes energy within 100 ns.

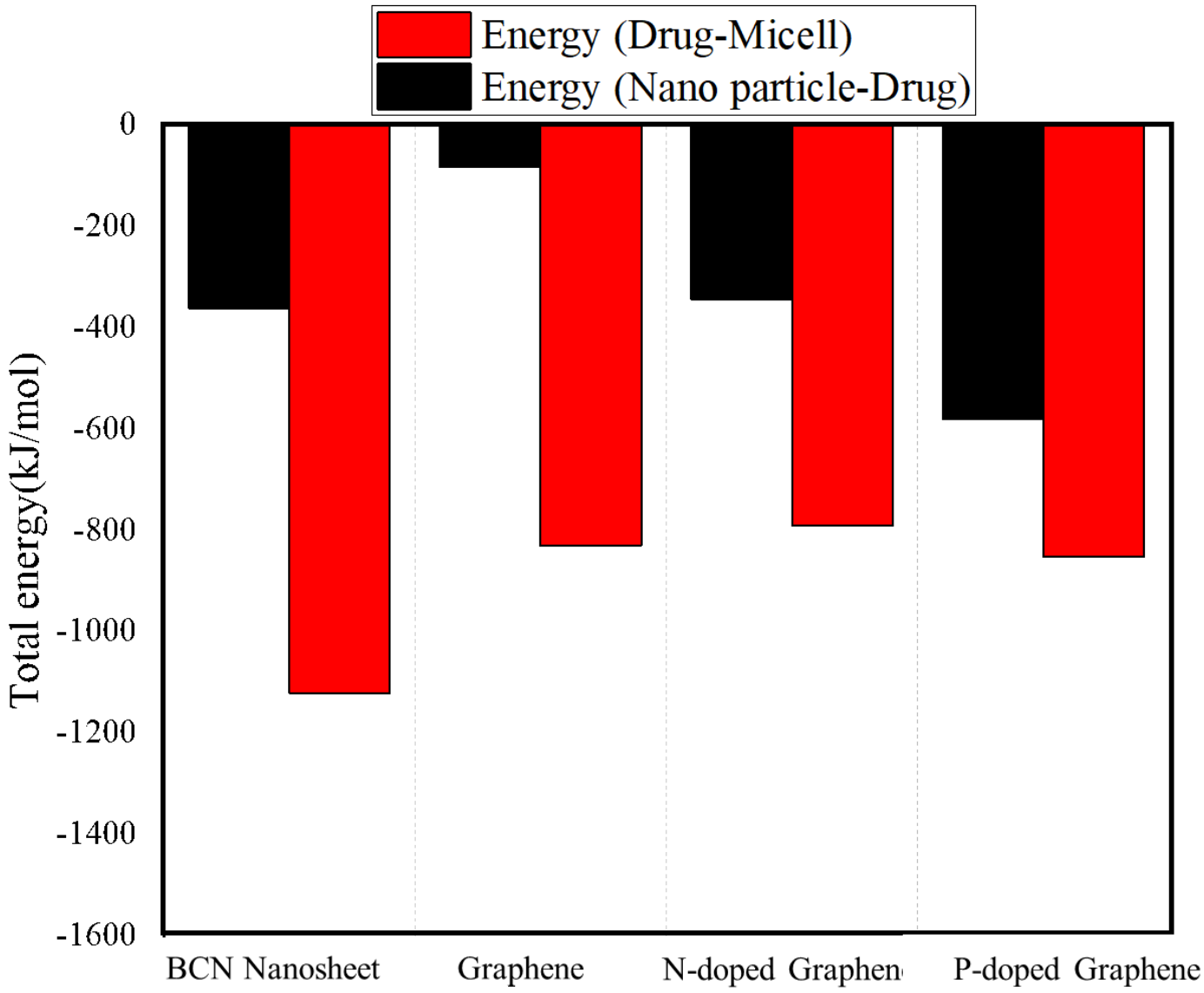

Figure 9

The contribution of vdW and electrostatic energies in the average drug-polymer micelles energy and the average drug- nanosheet energy within 100 ns.

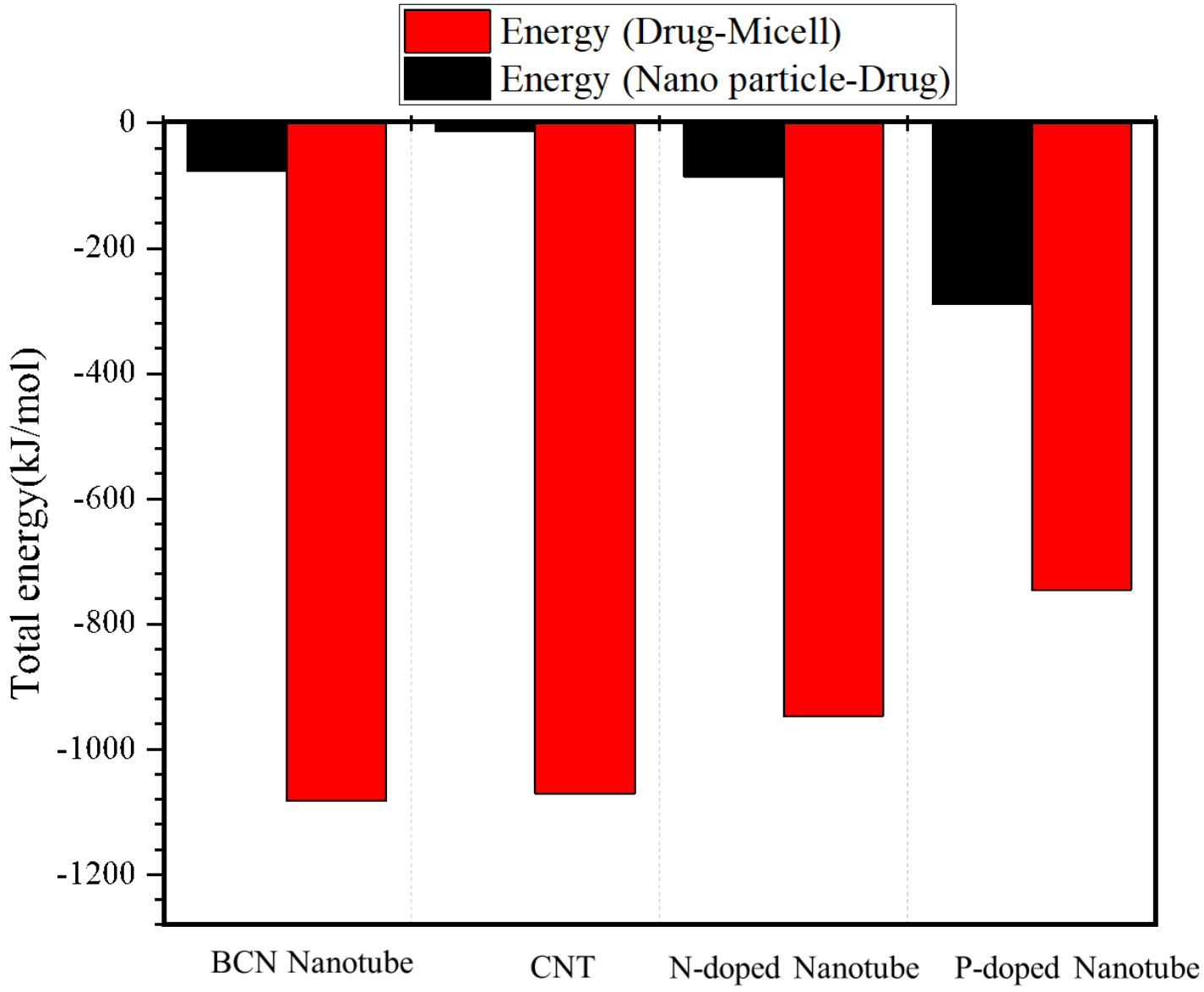

Figure 10

The contribution of vdW and electrostatic energies in the average drug-polymer micelles energy and the average drug-CNT energy within 100 ns.

Supplementary Files

This is a list of supplementary files associated with this preprint. Click to download.

- floatimage1.png